

Lens binarity vs limb darkening in close-impact galactic microlensing events

M. Dominik

University of St Andrews, School of Physics & Astronomy, North Haugh, St Andrews, KY16 9SS

17 November 2018

ABSTRACT

Although point caustics harbour a larger potential for measuring the brightness profile of stars during the course of a microlensing event than (line-shaped) fold caustics, the effect of lens binarity significantly limits the achievable accuracy. Therefore, corresponding close-impact events make a less favourable case for limb-darkening measurements than those events that involve fold-caustic passages, from which precision measurements can easily and routinely be obtained. Examples involving later Bulge giants indicate that a $\sim 10\%$ misestimate on the limb-darkening coefficient can result with the assumption of a single-lens model that looks acceptable, unless the precision of the photometric measurements is pushed below the 1%-level even for these favourable targets. In contrast, measurement uncertainties on the proper motion between lens and source are dominated by the assessment of the angular radius of the source star and remain practically unaffected by lens binarity. Rather than judging the goodness-of-fit by means of a χ^2 test only, run tests provide useful additional information that can lead to the rejection of models and the detection of lens binarity in close-impact microlensing events.

Key words: gravitational lensing – stars: atmospheres.

1 INTRODUCTION

In order to resolve the surface of the observed star during a microlensing event, the magnification pattern created by the lens needs to supply a large magnification gradient. Two such configurations meeting this requirement have been discussed extensively in the literature: a point-caustic at the angular position of a single point-like lens (Witt & Mao 1994; Nemiroff & Wickramasinghe 1994; Gould 1994; Bogdanov & Cherepashchuk 1995, 1996; Witt 1995; Gould & Welch 1996; Gaudi & Gould 1999; Heyrovský et al. 2000; Heyrovský 2003) and a line-shaped fold caustic produced by a binary lens (Schneider & Weiß 1987; Schneider & Wagoner 1987; Gaudi & Gould 1999; Rhie & Bennett 1999; Dominik 2004a,b,c). It has been pointed out by Gaudi & Gould (1999) that fold-caustic events are more common and their observation is easier to plan, whereas close-impact events where the source transits a point caustic can provide more information. However, I will argue that this apparent gain of information can usually not be realized due to potential lens binarity. In contrast to fold caustics which form a generically stable singularity, point caustics are not stable and do not exist in reality. Instead, there is always a small diamond-shaped caustic containing four cusps.

In this paper, the influence of lens binarity on the measurement of stellar limb-darkening coefficients and proper motion is investigated and the arising limitations of the power of close-impact events where the source passes over a single closed caustic are dis-

cussed. Sect. 2 discusses the basics of close-impact microlensing events with the effect of source size, the potential of measuring stellar proper motion and limb darkening, and the effect of lens binarity. Sect. 3 shows the influence of lens binarity on the extraction of information from such events. First, the effect of lens binarity on the light curves is demonstrated by means of two illustrative examples involving K and M Bulge giants. Subsequently, a simulation of data corresponding to these configurations is used to investigate the potential misestimates of parameters if lens binarity is neglected. Sect. 4 presents the final conclusions and a summary of the results.

2 CLOSE-IMPACT MICROLENSING EVENTS

2.1 Size of source star

As pointed out by Paczynski (1986), a point-like source star at a distance D_S from the observer exhibits a magnification due to the gravitational field of a lens star with mass M at D_L by a factor

$$A(u) = \frac{u^2 + 2}{u \sqrt{u^2 + 4}}, \quad (1)$$

where source and lens are separated by the angle $u \theta_E$ and

$$\theta_E = \sqrt{\frac{4GM}{c^2} \frac{D_S - D_L}{D_S D_L}} \quad (2)$$

denotes the angular Einstein radius.

The proper motion μ of the source relative to the lens constitutes a microlensing event with the time-scale $t_E = \theta_E/\mu$, for which the lens-source separation becomes

$$u(t) = \sqrt{u_0^2 + [p(t)]^2}, \quad (3)$$

where $p(t) = (t - t_0)/t_E$, so that u_0 is the closest approach which occurs at time t_0 .

It was discussed by Witt & Mao (1994) as well as by Nemiroff & Wickramasinghe (1994) that the finite extent of the source star could cause observable deviations from the magnification factor $A(u)$ as given by Eq. (1). Gould (1994) has argued that for a source star with radius $R_* = \rho_* \theta_E$ and radial brightness profile $I(\rho) = \bar{I} \xi(\rho)$, where ρ is the fractional radius and \bar{I} is the average brightness, the finite-source magnification can be approximated as

$$A^{\text{ext}}(u, \rho_*) = A(u) B(u/\rho_*; \xi), \quad (4)$$

with

$$B(z; \xi) = \frac{1}{\pi} \int_0^{2\pi} \int_0^1 \xi(\rho) \frac{z}{\sqrt{\rho^2 + 2\rho z \cos \varphi + z^2}} \rho d\rho d\varphi. \quad (5)$$

In particular, $B(z) \simeq 1$ for $z \gg 1$, so that for large angular separations (compared to ρ_*), the finite source effects becomes negligible, whereas $B(z) \simeq \beta z$ for $z \ll 1$ implies strong effects for small angular separations. Therefore, microlensing events with small impact parameters $u_0 \ll \rho$ are the most likely to show prominent effects of finite source size. Stellar spectra can be used to derive radius R_* and distance D_S of the source star, yielding its angular radius $\theta_* = R_*/D_S$. On the other hand, microlensing observations yield ρ_* and therefore the time-scale $t_* = \rho_* t_E$, during which the source moves by its own angular radius on the sky. Therefore, the observation of finite source effects in microlensing events provides a measurement of the proper motion between lens and source as

$$\mu = \frac{\theta_*}{t_*} = \frac{R_*}{D_S \rho_* t_E}. \quad (6)$$

2.2 Limb darkening

As already indicated, the stellar surface is not uniformly bright, but a characteristic variation with the distance from the center is observed, commonly known as limb darkening, which depends on wavelength and therefore on the filter used for the observations. A widely used model is the linear limb-darkening law (Milne 1921)

$$\xi(\rho) = 1 + \Gamma \left(\frac{3}{2} \sqrt{1 - \rho^2} - 1 \right), \quad (7)$$

with $0 \leq \Gamma \leq 1$, which is linear in $\cos \vartheta = \sqrt{1 - \rho^2}$, where ϑ is the emergent angle. If the point-source magnification $A(u)$ shows a strong variation over the face of the source star, dense and precise microlensing observations provide an opportunity for a measurement of the limb-darkening coefficient (Bogdanov & Cherepashchuk 1996; Gould & Welch 1996).

The strongest magnification gradients occur in the vicinity of caustics. While a single lens creates a point caustic at its angular position, binary lenses create finite caustic curves which contain cusps. As the angular separation between the binary lens objects tends to zero, its diamond-shaped caustic with four cusps degenerates into the point caustic of a single lens. There are two different main scenarios with the potential of providing limb-darkening measurements: passages of the source star over the point caustic of a single lens, so that the

impact parameter falls below the angular source radius, i.e. $u_0 < \rho_*$ (Bogdanov & Cherepashchuk 1996; Gould & Welch 1996; Gaudi & Gould 1999; Heyrovský et al. 2000; Heyrovský 2003), and passages of the source star over a (line-shaped) fold caustic created by a binary lens (Schneider & Weiß 1987; Schneider & Wagoner 1987; Gaudi & Gould 1999; Rhie & Bennett 1999; Dominik 2004a,c). In addition, the source might pass directly over a cusp, as for the event MA-CHO 1997-BLG-28 (Albrow et al. 1999b), for which the first limb-darkening measurement by microlensing has been obtained. As anticipated by Gaudi & Gould (1999), the vast majority of other limb-darkening measurements so far has arisen from fold-caustic passages (Afonso et al. 2000; Albrow et al. 2000, 2001; Fields et al. 2003), whereas two measurements from single-lens events have been reported so far (Alcock et al. 1997; Yoo et al. 2004). The remaining limb-darkening measurement by microlensing, on the solar-like star MOA 2002-BLG-33 Abe et al. (2003) constituted a very special case, where the source simultaneously enclosed several cusps over the course of its passage.

2.3 Lens binarity

Since the majority of stars resides in some form of binary or multiple systems (e.g. Abt 1983), it seems at first sight a bit surprising that more than 85 % of the observed microlensing events appear to be consistent with the assumption of a single point-like lens. An important clue to this puzzle is that the separation of binaries covers a broad range of 6–7 orders of magnitude roughly from contact to typical stellar distances. Lens binarity however usually does not provide strong deviations to the light curve if the angular separation is much smaller or much larger than the angular Einstein radius θ_E (Mao & Paczynski 1991). Therefore, many binary lenses simply escape our attention by failing to provide an observable signal (Di Stefano 2000). While several binary lens systems provide weak distortions, such as MACHO LMC-1 (Dominik & Hirshfeld 1994, 1996) or MACHO 1999-BLG-47 (Albrow et al. 2002), a characteristic signature is provided if the source passes over a fold or even a cusp caustic, OGLE-7 (Udalski et al. 1994) being the first such observed event.

Thus, although a lens star is never a completely isolated object, it can be approximated as such in many cases. However, one needs to keep in mind that its caustic is a small diamond with four cusps rather than a single point. While for a single lens, the computation of the light curve is a rather straightforward process, where a semi-analytical expression by means of elliptical integral exists for uniformly bright sources (Witt & Mao 1994), it becomes quite demanding if a binary lens is considered due to the fact that no closed expression exists for the point-source magnification of a binary lens, but in general a fifth-order polynomial needs to be solved (Witt & Mao 1995; Asada 2002). For this paper, the algorithm of Dominik (1998) has been used which is based on the contour plot technique by Schramm & Kayser (1987) and the application of Green's theorem.

Compared to a single lens, a binary lens involves three additional parameters, which can be chosen as the mass ratio q , the angle α , and the separation parameter d . Here, $q = M_2/M_1$ is the ratio between the masses of secondary and the primary component which are separated on the sky by the angle $d\theta_E$, while α is measured from the vector pointing from the secondary to the primary towards the source trajectory which therefore reads

Table 1. Model parameters and indicative corresponding physical properties for the two discussed event configurations.

	configuration I	configuration II
t_E [d]	55	35
t_0 [d]	0	0
u_0	0.015	0.05
ρ_*	0.05	0.075
α	0°	0°
q	1	1
I_{base}	13.6	12.3
g	0	0
Γ_I	0.5	0.5
D_S [kpc]	~ 8.5	~ 8.5
D_L [kpc]	~ 6.5	~ 6.5
M [M_\odot]	~ 0.35	~ 0.7
v [km s^{-1}]	~ 55	~ 140
μ [$\mu\text{as d}^{-1}$]	~ 330	~ 460
θ_E [μas]	~ 6	~ 15
r_E [AU]	~ 2.0	~ 2.9
r'_E [R_\odot]	~ 500	~ 800
R_* [R_\odot]	~ 25	~ 60
spectral type	K5III	M4III
M_V	-0.2	+0.2
$V - I$	+2.0	+3.4
A_I	1.25	0.85
$m - M$	14.65	14.65

$$\mathbf{u}(t) = u_0 \begin{pmatrix} -\sin \alpha \\ \cos \alpha \end{pmatrix} + p(t) \begin{pmatrix} \cos \alpha \\ \sin \alpha \end{pmatrix}. \quad (8)$$

3 BINARITY VS LIMB DARKENING

3.1 Illustrative binary-lens configurations

In order to investigate the effect of lens binarity on the measurement of stellar limb darkening and proper motion, two different event configurations have been chosen as illustrative examples, where different angular separations between the lens objects have been considered for both of them. For the model referred to as 'configuration I', let us consider a K5 Bulge giant at $D_S \sim 8.5$ kpc, for which $M_V = -0.2$ and $V - I = +2.0$. One therefore obtains $I_0 = 12.35$, so that with an assumed extinction $A_I \sim 1.25$, the observed source magnitude becomes $I \sim 13.6$. Let us further assume a binary lens of total mass $M \sim 0.35 M_\odot$ at $D_L \sim 6.5$ kpc, so that the angular Einstein radius becomes $\theta_E \sim 320 \mu\text{as}$, the Einstein radius becomes $r_E = D_L \theta_E \sim 2.0$ AU and its projection to the source distance becomes $r'_E = (D_S/D_L) r_E \sim 500 R_\odot$. With $R_* \sim 25 R_\odot$ for a K5 giant, a source size parameter $\rho_* = 0.05$ is therefore adopted. In order to make an optimal case for observing, a rather low proper motion $\mu \sim 6 \text{ km s}^{-1}$, corresponding to a lens velocity of $v \sim 55 \text{ km s}^{-1}$ relative to the source has been chosen, which yields an event time-scale $t_E = 55$ d. The impact parameter is chosen as $u_0 = 0.015$, corresponding to a peak magnification of a point source of $A_0 \sim 70$.

Configuration II has been chosen to be similar to the parameters of the observed event MACHO 1995-BLG-30 (Alcock et al. 1997), for which the source is an even larger star, namely an M4 giant. According to the obtained model parameters, let us adopt $u_0 = 0.05$, $\rho_* = 0.075$, and the event time-scale $t_E = 35$ d. For $D_S \sim 8.5$ kpc and $D_L \sim 6.5$ kpc, the appropriate stellar radius

of $R_* \sim 60 R_\odot$ is obtained for $M \sim 0.7 M_\odot$, so that $r'_E \sim 800 R_\odot$. These choices yield $r_E \sim 2.9$ AU and $\theta_E \sim 460 \mu\text{as}$, so that the proper motion becomes $\mu \sim 15 \text{ km s}^{-1}$ and the relative lens velocity is $v \sim 140 \text{ km s}^{-1}$. With $M_V = +0.2$ and $V - I = +3.4$ for an M4 giant, an extinction of $A_I = 0.85$ yields the baseline magnitude $I_{\text{base}} = 12.3$.

Binary lenses are likely to cause an asymmetry to the light curve, which however can be arbitrarily small and can even vanish for some configurations. In order to study the maximal impact of binarity on the measurement of limb darkening, configurations have been chosen that preserve the symmetry. Therefore, let us assume that both lens objects have the same mass and consider a source trajectory parallel to the line connecting their angular positions.

In general, the light received from the source is blended with additional light from other unresolved sources (that are not affected by microlensing) or from the lens star, which is quantified by the blend ratio $g = F_B/F_S$, where F_S denotes the source flux and F_B denotes the background (blend) flux. Since the choice of equal lens masses implies that the lens objects are M dwarfs of mass $M/2 \sim 0.18 M_\odot$ or $M/2 \sim 0.35 M_\odot$, their contribution to the total light falls well below the systematic error bars even at the observed I -baseline. Therefore, blending is neglected with the choice $g = 0$. Finally, a limb-darkening coefficient $\Gamma_I = 0.5$ has been adopted for both configurations.

The model parameters and indicative corresponding physical properties of matching lens and source stars are summarized in Table 1. Light curves that correspond to either of the adopted configurations are shown in Fig. 1 for a binary-lens separation parameter $d = 0.2$ along with light curves that correspond to single-lens models with otherwise identical parameters, while Fig. 2 shows the difference in magnitude between these lightcurves. Lens binarity decreases the magnification both around the peak and in the wing region, while an increase in magnification results in regions just before the lens center is hit by the leading limb or just after it is hit by the trailing limb. For configuration I, these regions of increased magnification stretch over a much larger part of the light curve than the corresponding regions for configuration II.

If we assume the lens center-of-mass as the origin of coordinates and the angular Einstein radius θ_E as the unitlength, and if we choose the separation vector of the binary lens objects along the x -axis, the four cusps of its central caustic are found at

$$\begin{aligned} \mathbf{s}_\leftarrow &= (s_1^-, 0), & \mathbf{s}_\rightarrow &= (s_1^+, 0), \\ \mathbf{s}_\uparrow &= (\Delta s, s_2), & \mathbf{s}_\downarrow &= (\Delta s, -s_2). \end{aligned} \quad (9)$$

For a point source, these four cusps degenerate into the single point $\mathbf{s}_0 = 0$, placing the caustic entry and exit at

$$p_0^\pm(t) = \sqrt{\rho_*^2 - u_0^2}. \quad (10)$$

The coordinates for which the leading or trailing limb of the source hits a cusp then follow from the condition $[\mathbf{u}(t) - \mathbf{s}]^2 = \rho_*^2$, with $\mathbf{u}(t)$ given by Eq. (8), as

$$\begin{aligned} p_-^\pm(t) &= s_1^- \cos \alpha \pm \sqrt{\rho_*^2 - (u_0 + s_1^- \sin \alpha)^2}, \\ p_+^\pm(t) &= s_1^+ \cos \alpha \pm \sqrt{\rho_*^2 - (u_0 + s_1^+ \sin \alpha)^2}, \\ p_\uparrow^\pm(t) &= s_2 \sin \alpha + \Delta s \cos \alpha \pm \\ &\quad \pm \sqrt{\rho_*^2 - (u_0 - s_2 \cos \alpha + \Delta s \sin \alpha)^2}, \\ p_\downarrow^\pm(t) &= -s_2 \sin \alpha + \Delta s \cos \alpha \pm \\ &\quad \pm \sqrt{\rho_*^2 - (u_0 + s_2 \cos \alpha + \Delta s \sin \alpha)^2}. \end{aligned} \quad (11)$$

For equal masses ($q = 1$), $s_1^+ = -s_1^- = s_1$ and $\Delta s = 0$, while

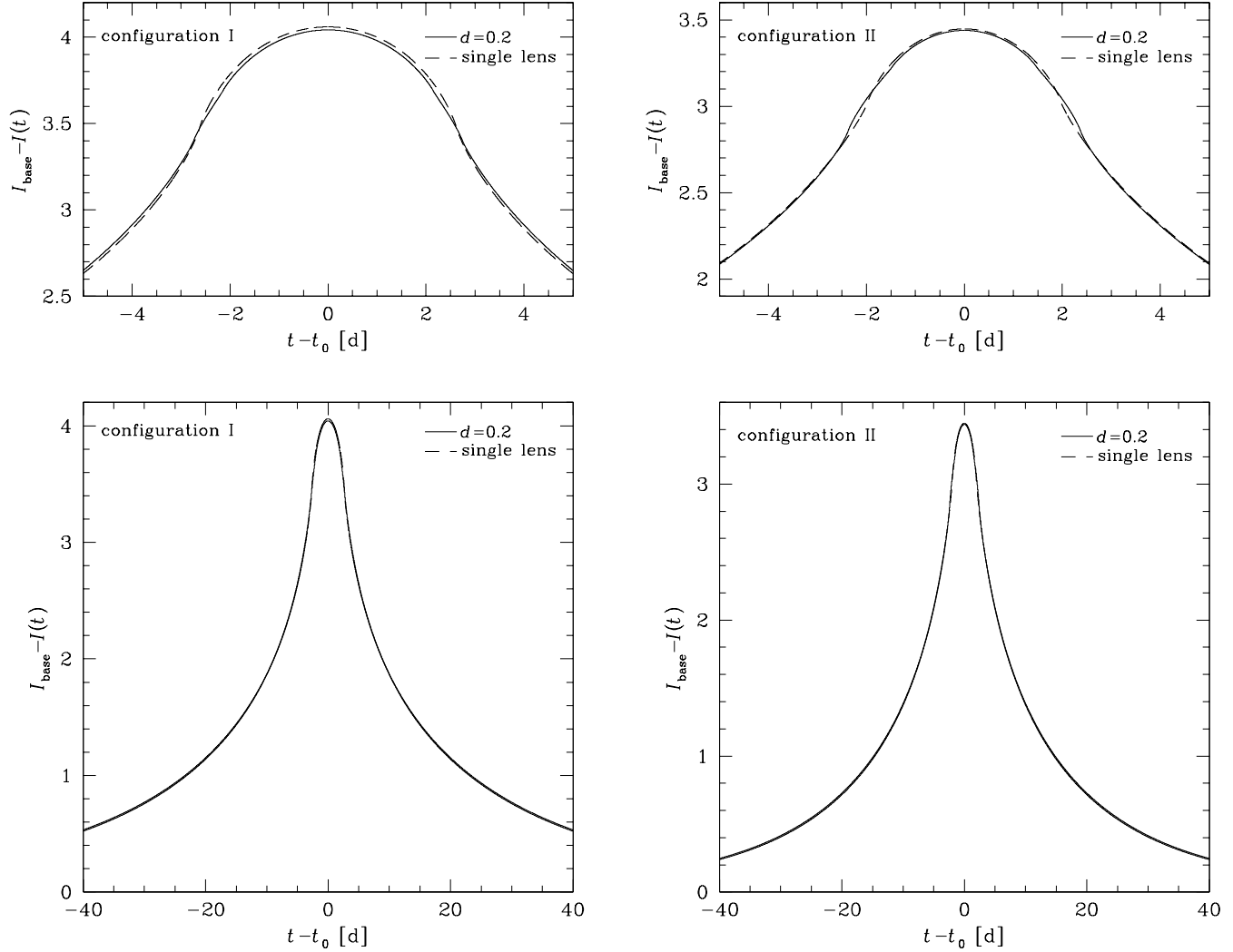


Figure 1. Light curves corresponding to the binary-lens configuration I (left) and configuration II (right) with parameters as listed in Table 1 and a separation parameter $d = 0.2$ (solid line) along with those for a single lens model with otherwise identical parameters (dashed line). In the lower panels, which show the full wing of the light curves, binary-lens and single-lens models are hardly distinguishable.

for a point source, the four cusps degenerate into the point $s_0 = 0$, placing the caustic entry and exit at

$$p_0^\pm(t) = \sqrt{\rho_\star^2 - u_0^2}. \quad (12)$$

The passage of the leading stellar limb over the cusps is illustrated in Fig. 3, which shows snapshots of the source and the caustic for $d = 0.2$ and both configurations at times t_\leftarrow^- , t_\rightarrow^- , t_\leftarrow^+ , or t_\rightarrow^+ , which correspond to the source positions p_\leftarrow^- , p_\rightarrow^- , p_\leftarrow^+ , or p_\rightarrow^+ , respectively, along with the light curve for $-4 \text{ d} \leq t \leq 0$. Dashed lines refer to t_0^- , corresponding to p_0^- , which is the beginning of the caustic passage for a single point lens.

With the source size parameter ρ_\star being larger for configuration II, a smaller fraction of the source is subtended by the caustic for the same choice of the lens separation parameter d . A larger impact parameter u_0 places the effect of binarity more towards the limb of the source. Despite a larger source size parameter ρ_\star , the combination of a smaller impact parameter u_0 and a smaller event time-scale t_E leads to a shorter caustic passage time, which, for a single lens, is $t_0^+ - t_0^- \sim 3.9 \text{ d}$ for configuration II compared to $t_0^+ - t_0^- \sim 5.2 \text{ d}$ for configuration I.

On the inclusion of a cusp, the leading limb may enter the

caustic, exit the caustic, or just touch it there so that the tangents of the circle and the merging fold lines match. For $d = 0.2$ and configuration II, the caustic is entered for p_\leftarrow^- and p_\rightarrow^- , whereas it is exited for p_\leftarrow^+ and p_\rightarrow^+ . In contrast, the caustic is exited for p_\rightarrow^- for configuration I and the same lens separation. A sign change in the curvature of the light curve similar to that for a single lens near t_0^\pm is seen for the binary-lens light curves near t_\leftarrow^\pm , whereas all other cusp intersections are not that easily identified by observable features in the light curve.

3.2 Simulated sampled light curves

In order to see what kind of information can be extracted from sampled light curves, simulated data sets have been created that correspond to the two chosen binary-lens configurations. The event sampling parameters for this simulation have been chosen in analogy to an earlier investigation of fold-caustic passages (Dominik 2004c). For data in the range $t_{\min} \leq t \leq t_{\max}$, the sampling is characterized by the sampling interval Δt , the fluctuation $f_{\Delta t}$ of the time at which the measurement is taken, and the relative sampling phase shift f_{phase} , where values of $f_{\Delta t} = 1/6$ and $f_{\text{phase}} = 0.2$ have

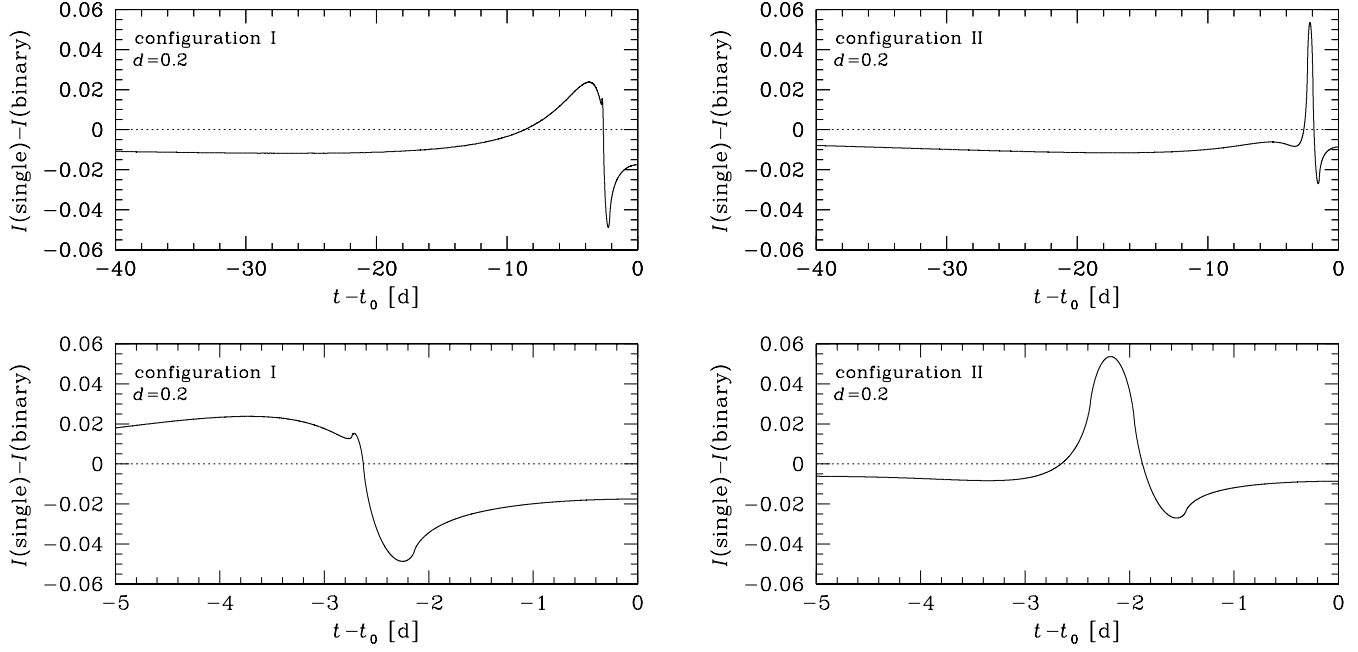


Figure 2. Difference between binary-lens light curves with the angular separation parameter $d = 0.2$ for configuration I (left) or configuration II (right) and their single-lens counterparts.

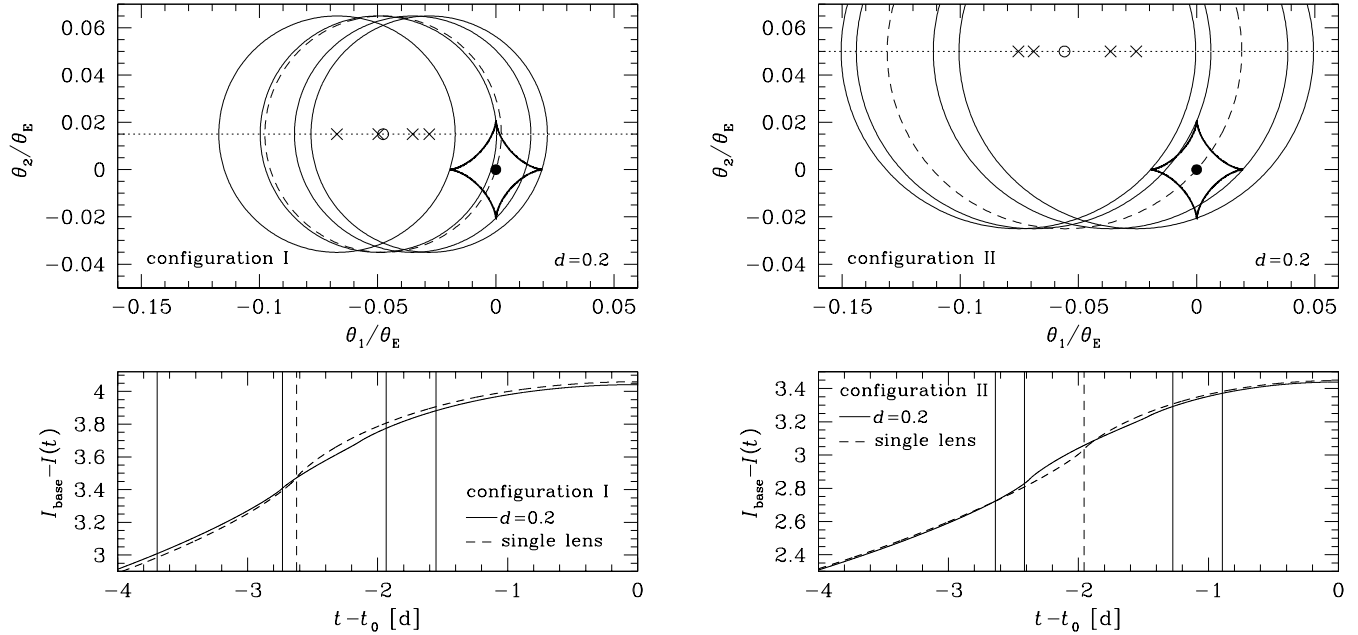


Figure 3. Passages of the leading limb of the source over the four cusps for configuration I (left) or configuration II (right) and a binary-lens separation of $d = 0.2$. The upper panels show the caustic (bold line) and the lens center (filled circle) with snapshots of the source as the trailing limb hits a cusp, as well as it touches the lens center (dashed line). The dotted line indicates the track of the source, while diagonal crosses mark the position when a cusp is hit, whereas the passage of the lens center is indicated by an open circle. For configuration I, the leading limb touches the caustic for $p_{\leftarrow}^- = -0.0672$, $p_{\rightarrow}^- = -0.0497$, $p_{\downarrow}^- = -0.0352$, or $p_{\uparrow}^- = -0.0282$ (in this order), corresponding to times $t_{\leftarrow}^- = -3.696$ d, $t_{\rightarrow}^- = -2.733$ d, $t_{\downarrow}^- = -1.935$ d, or $t_{\uparrow}^- = -1.551$ d relative to t_0 , while the lens center is hit for $p_0^- = -0.0477$, i.e. at $t_0^- = -2.623$ d. For configuration II, the leading limb touches the cusps for $p_{\leftarrow}^- = -0.0754$, $p_{\rightarrow}^- = -0.0690$, $p_{\downarrow}^- = -0.0364$, or $p_{\uparrow}^- = -0.0255$ (in this order), and hits the lens center for $p_0^- = -0.0559$, which corresponds to times $t_{\leftarrow}^- = -2.639$ d, $t_{\rightarrow}^- = -2.4163$ d, $t_{\downarrow}^- = -1.274$ d, $t_{\uparrow}^- = -0.894$ d, and $t_0^- = -1.957$ d relative to t_0 . In contrast to configuration I, the order between p_{\rightarrow}^- and p_{\downarrow}^- is reversed. The lower panels show the lightcurve for the binary lens (solid line) together with that for a point lens with otherwise identical parameters (dashed line), where t_{\leftarrow}^- , t_{\rightarrow}^- , t_{\downarrow}^- , and t_{\uparrow}^- are indicated by thin solid lines, and t_0^- is indicated by a thin dashed line.

Table 2. Sampling intervals and number of data points for configuration I

t_{\min} [d]	t_{\max} [d]	Δt	N
0	3	20 min	405
3	6	30 min	271
6	20	1 h	636
20	30	2 h	226
30	60	6 h	227
60	100	12 h	153
100	150	1 d	95
150	300	2 d	142

With $t_0 = 0$, a constant sampling rate has been adopted on both sides of the peak for intervals $-t_{\max} \leq t \leq -t_{\min}$ and $t_{\min} \leq t \leq t_{\max}$. Due to the applied phase shift f_{phase} and the fluctuation of the time when the observations are taken, $f_{\Delta t}$, the actual times of observation may fall outside the originally designated interval. N denotes the number of data points for each selected t_{\min} and t_{\max} . In total, 2155 data points have been created.

Table 3. Sampling intervals and number of data points for configuration II

t_{\min} [d]	t_{\max} [d]	Δt	N
0	3	20 min	405
3	5	30 min	181
5	10	1 h	227
10	20	2 h	227
20	40	4 h	227
40	60	6 h	152
60	80	12 h	79
80	120	1 d	75
120	300	2 d	168

Same as Table 2 for configuration II, where a total of 1741 data points have been created.

been adopted here. The sampling intervals Δt for different regions of the light curve have been chosen to roughly comply with the observing strategy of the PLANET microlensing follow-up campaign (Albrow et al. 1998; Dominik et al. 2002) for the central region and with that of the OGLE-III survey (Udalski 2003) for the outer regions. These are listed in Tables 2 and 3.

For a reference magnitude of $m_{\text{ref}} = 16$ in I -band, an uncertainty of $\sigma_{\text{ref}} = 0.015$ in the observed magnitude has been assumed, corresponding to a $\sim 1.5\%$ relative uncertainty in the measured flux. For other magnitudes, it is assumed that the photometric measurement follows Poisson statistics, so that its uncertainty is proportional to the square-root of the observed flux. This uncertainty has been smeared with a relative standard deviation of $f_{\sigma} = 0.125$. The resulting photometric error bar σ_{phot} yet does not represent the total measurement uncertainty. Instead, a systematic error σ_0 is added in quadrature, which becomes dominant as the target gets bright. For the systematic error, three different values $\sigma_0 = 0.3\%$, $\sigma_0 = 0.5\%$, or $\sigma_0 = 1\%$ have been used.

All the above choices mean that the creation of synthetic data sets $(t^{(i)}, m^{(i)}, \sigma^{(i)})$ follows the rules

$$t^{(i)} = \mathcal{N}[t_{\min} + (i + f_{\text{phase}}) \Delta t, f_{\Delta t} \Delta t], \quad (13)$$

$$\bar{\sigma}^{(i)} = \sigma_{\text{ref}} 10^{0.2[m(t^{(i)}) - m_{\text{ref}}]}, \quad (14)$$

$$\sigma_{\text{phot}}^{(i)} = \mathcal{N}(\bar{\sigma}^{(i)}, f_{\sigma} \bar{\sigma}^{(i)}), \quad (15)$$

$$\sigma^{(i)} = \sqrt{\left[\sigma_{\text{phot}}^{(i)}\right]^2 + \sigma_0^2}, \quad (16)$$

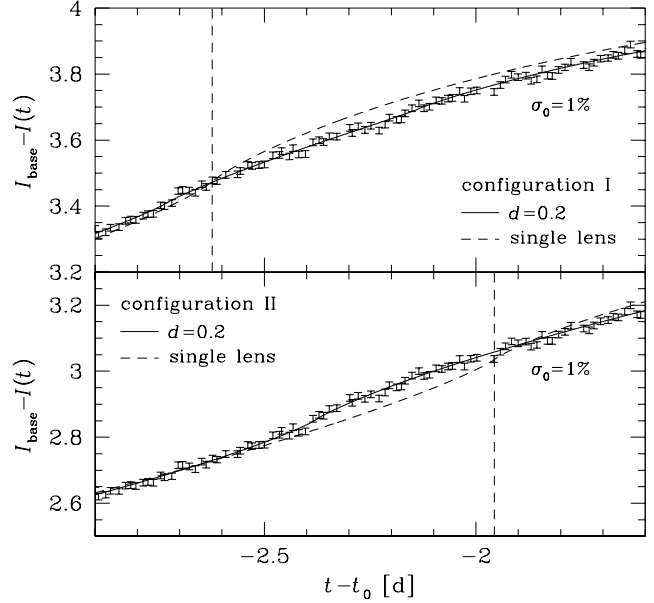


Figure 4. Binary-lens light curves (solid line) and simulated data for $\sigma_0 = 1\%$ for both configurations and a lens separation parameter $d = 0.2$. Also shown are light curves for corresponding single-lens models with otherwise identical parameters (dashed line). The time t_0^- at which the leading limb hits the single-lens point caustic is indicated by a vertical thin dashed line.

$$m^{(i)} = \mathcal{N}(m(t^{(i)}), \sigma^{(i)}), \quad (17)$$

where $\mathcal{N}(\mu, \sigma)$ denotes a value drawn randomly from a normal distribution with mean μ and standard deviation σ , $m(t^{(i)})$ denotes the magnitude at time $t^{(i)}$ for the adopted model parameters, and $i \in [0, (t_{\max} - t_{\min})/(\Delta t)]$.

In order to simulate possible losses in the data acquisition due to observing conditions or technical problems, data points have been removed from the dataset at random with a probability of $p_{\text{loss}} = 5\%$.

In fact, a round-the-clock coverage (without daylight gaps) requires more than one telescope. Nevertheless, the effects of additional free parameters (mainly baselines magnitudes) and different telescope characteristics for multi-site observations are neglected in favour of simplicity, and the data is treated such as resulting from a single telescope.

The quality of coverage of the data set is demonstrated in Fig. 4, which shows the simulated data points and the theoretical light curves for $d = 0.2$ and $\sigma_0 = 1\%$ for both binary-lens configurations around the contact of the leading limb with the lens center. To indicate the influence of lens binarity, the corresponding single-lens light curves are also shown.

3.3 Best-matching single-lens models

Let us now assume a single lens and determine the corresponding model parameters by means of fits to the simulated data sets that correspond to the two binary-lens configurations. We will then see whether statistical tests suggest to accept the single-lens model and how well the true limb-darkening coefficient Γ and the time-scale t_* , which yields the proper motion as $\mu = \theta_*/t_*$, are reproduced. Any significant offsets for acceptable single-lens models will limit the accuracy to which these parameters are determined on the assumption of such a model.

Tables 4 and 5 list the obtained model parameters and the re-

Table 4. Best-matching single-lens models to configuration I binary-lens models with different angular lens separations for different systematic errors.

	$\sigma_0 = 0.3\%$			$\sigma_0 = 0.5\%$			$\sigma_0 = 1\%$		
	$d = 0.2$	$d = 0.15$	$d = 0.1$	$d = 0.2$	$d = 0.15$	$d = 0.1$	$d = 0.2$	$d = 0.15$	$d = 0.1$
χ^2_{\min}	18054.9	4337.6	2235.6	8873.9	2969.9	2097.89	3895.1	2267.8	2037.6
d.o.f.	2149	2149	2149	2149	2149	2149	2149	2149	2149
$\chi^2_{\min}/\text{d.o.f.}$	8.40	2.02	1.04	4.13	1.38	0.976	1.81	1.06	0.948
$\sqrt{2\chi^2_{\min} - \sqrt{2n-1}}$	124.5	27.6	1.32	67.7	11.5	-0.78	22.7	1.80	-1.72
$P(\chi^2 \geq \chi^2_{\min})$	$\lesssim 10^{-3366}$	$\lesssim 10^{-167}$	0.094	$\lesssim 10^{-996}$	$\lesssim 10^{-30}$	0.781	$\lesssim 10^{-113}$	0.037	0.957
t_E	55.44	54.99	54.93	55.28	54.94	54.91	55.18	54.91	54.91
u_0	0.0157	0.0149	0.0148	0.0155	0.0148	0.0147	0.0153	0.0148	0.0147
ρ_*	0.0541	0.0518	0.0503	0.0542	0.0519	0.0503	0.0543	0.0520	0.0503
I_{base}	13.609	13.604	13.601	13.608	13.604	13.602	13.607	13.603	13.602
Γ_I	1.000	0.746	0.538	1.000	0.751	0.538	1.000	0.751	0.537

The complete data set has been included. The 'true' binary-lens parameters are shown in Table 1. The blending parameter has been fixed to $g = 0$, whereas t_0 has been allowed to vary, yielding $|t_0| \lesssim 90$ s in all cases. The quantity $\sqrt{2\chi^2_{\min} - \sqrt{2n-1}}$ is a measure of the goodness-of-fit as a characteristic of a χ^2 -test yielding the equivalent deviation from the mean in units of the standard deviation for a Gaussian distribution, where n is the number of degrees of freedom (d.o.f.), which is the number of data points reduced by the number of free model parameters, while $P(\chi^2 \geq \chi^2_{\min})$ denotes the associated probability.

Table 5. Best-matching single-lens models to configuration II binary-lens models with different angular lens separations for different systematic errors.

	$\sigma_0 = 0.3\%$			$\sigma_0 = 0.5\%$			$\sigma_0 = 1\%$		
	$d = 0.2$	$d = 0.15$	$d = 0.1$	$d = 0.2$	$d = 0.15$	$d = 0.1$	$d = 0.2$	$d = 0.15$	$d = 0.1$
χ^2_{\min}	5670.3	2371.2	1791.5	3161.4	1895.0	1666.8	2001.6	1668.7	1605.0
d.o.f.	1735	1735	1735	1735	1735	1735	1735	1735	1735
$\chi^2_{\min}/\text{d.o.f.}$	3.27	1.37	1.03	1.82	1.09	0.961	1.15	0.962	0.925
$\sqrt{2\chi^2_{\min} - \sqrt{2n-1}}$	47.6	10.0	0.96	20.6	2.66	-1.16	4.4	-1.13	-2.24
$P(\chi^2 \geq \chi^2_{\min})$	$\lesssim 10^{-494}$	$\lesssim 10^{-23}$	0.168	$\lesssim 10^{-94}$	0.004	0.877	$\lesssim 10^{-5}$	0.871	0.988
t_E	34.62	34.76	34.91	34.62	34.77	34.91	34.64	34.78	34.93
u_0	0.0489	0.0491	0.0497	0.0489	0.0491	0.0497	0.0489	0.0491	0.0497
ρ_*	0.0817	0.0795	0.0758	0.0817	0.0796	0.0758	0.0816	0.0796	0.0757
I_{base}	12.302	12.301	12.301	12.302	12.301	12.301	12.302	12.302	12.301
Γ_I	1.000	0.984	0.607	1.000	0.997	0.605	1.000	1.000	0.599

The same quantities as in Table 4 are displayed. Again, all data points have been included in the fits and the 'true' binary-lens parameters are listed in Table 1. The blending parameter has been fixed to $g = 0$, while t_0 was allowed to vary, where $|t_0| \lesssim 90$ s resulted in all cases.

sults of χ^2 tests for both binary-lens configurations and the different lens separations d and systematic errors σ_0 . For configuration I, χ^2 tests recommend to accept the single-lens model for $d = 0.1$ and all applied systematic errors, and marginally for $d = 0.15$ and $\sigma = 1\%$. The limb-darkening coefficient Γ_I turns out to be $\sim 8\%$ larger for $d = 0.1$, $\sim 50\%$ larger for $d = 0.15$, and tends to its maximal value $\Gamma_I = 1$ for $d = 0.2$. Compared to Γ_I , the relative offsets on t_* are much smaller, namely $\sim 0.5\%$ for $d = 0.1$, $\sim 4\%$ for $d = 0.15$, and $\sim 10\%$ for $d = 0.2$, usually below the uncertainty in the measurement of θ_* .

Similar to configuration I, the acceptance of the single-lens model for $d = 0.1$ and all applied systematic errors as well as for $d = 0.15$ and $\sigma = 1\%$ is recommended by χ^2 tests for configuration II. A larger goodness-of-fit than for configuration I comes along with a larger offset in Γ_I , namely $\sim 20\%$ for $d = 0.1$, while $\Gamma_I \sim 1$ is already reached for $d = 0.15$. The time-scale t_* is found to be shifted by $\sim 0.8\%$ for $d = 0.1$, $\sim 5\%$ for $d = 0.15$, and $\sim 8\%$ for $d = 0.2$,

The difference between the light curves for best-matching single-lens models and the 'true' binary-lens configuration for the three lens separations $d = 0.2$, $d = 0.15$, or $d = 0.1$ is shown in

Fig. 5. As Tables 4 and 5 show, the model parameters differ only very slightly for the different choices of the systematic error σ_0 , so that the corresponding light curves are practically identical. For Fig. 5, $\sigma_0 = 0.3\%$ has been chosen. For configuration I, some of the discrepancy is moved into the wing region of the light curve, where differences of up to 2% (for $d = 0.2$), 0.7% (for $d = 0.15$) or 0.2% (for $d = 0.1$) occur. In contrast, for configuration II, the maximal differences in the wing region are only 0.25% (for $d = 0.2$), 0.13% (for $d = 0.15$) or 0.1% (for $d = 0.1$). This reflects the fact that the region for which the binary-lens magnification exceeds that of a single lens extends significantly outside the region where the stellar limb touches the caustic for configuration I, while this is not the case for configuration II. The most significant deviations occur around times when the stellar limb touches the caustic, which are however below 3% (for $d = 0.2$), 2% (for $d = 0.15$) or 1.2% (for $d = 0.1$) for configuration I, and below 2.5% (for $d = 0.2$), 1% (for $d = 0.15$) or 0.8% (for $d = 0.1$) for configuration II.

Since it is quite challenging to achieve photometric uncertainties below the 1%-level, one should consider the effect of lens binarity as a serious problem for measuring limb-darkening coefficients

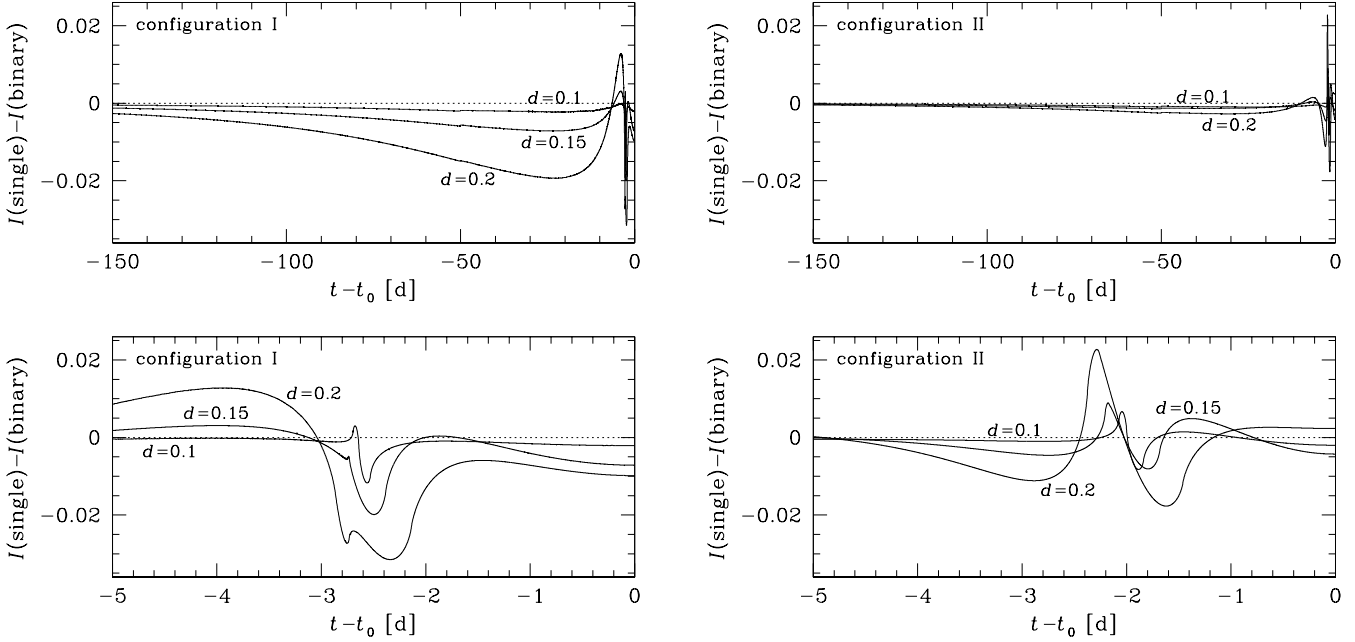


Figure 5. Differences in the light curve between a binary-lens model and a best-matching single lens model. The binary-lens models shown correspond to configuration I (left) or configuration II (right) and separations of $d = 0.2$, $d = 0.15$, and $d = 0.1$, while the single-lens model is the best fit for $\sigma_0 = 0.3\%$ as listed in Table 4 or Table 5, respectively. The upper panels show the full wing of the light curve, whereas the lower panels show only the peak region.

from close-impact microlensing events and be quite careful with results obtained under the assumption of a single lens.

An additional complication arises from the fact that photometric error bars reported by reduction algorithms such as DoPhot (Schechter et al. 1993) tend to underestimate the true photometric uncertainty for microlensing observations, which are plagued by varying observing conditions during the course of an event. Apart from the systematic error that is taken into account for the simulated data set, underestimates of 10–20 % occur frequently (e.g. Udalski et al. 1994; Albrow et al. 1998; Tsapras et al. 2003), so that the ratio $\chi^2/\text{d.o.f.}$ is not unlikely to exceed 1.4. This strongly limits the significance of the χ^2 test as a measure of the goodness-of-fit.

If one accepts an underestimate by 20 %, the single-lens model for the configuration I binary-lens data with $d = 0.15$ and $\sigma = 0.5\%$ becomes acceptable, while for configuration II, single-lens models look acceptable for $d = 0.15$ and all applied systematic errors as well as for $d = 0.2$ and $\sigma = 1\%$.

In addition to fits making use of the complete set of data points, best-matching single-lens models for the peak region of the lightcurve, defined as $-3 \text{ d} \leq t \leq 3 \text{ d}$, have been obtained for $\sigma_0 = 0.3\%$, for which the model parameters and the result of χ^2 tests are displayed in Table 6. In contrast to the fits recognizing the full data set, the baseline I_{base} has been fixed to its ‘true’ value, while the blending parameter g has been allowed to vary. As one could have expected from the larger discrepancies being attributed to the wing regions of the light curves for configuration I, the model parameters for the fits restricted to the peak region deviate more strongly from those obtained when the full data set is considered. In order to adjust to the optimal model, the blending parameter g has assumed a significant non-zero value. For all selected binary-lens separations d for configuration II and for $d = 0.1$ for configuration I, the goodness-of-fit resulting from the χ^2 test for the peak region model and data is worse than for the models and data for the full light curve, so that a rejection of all considered single-lens models

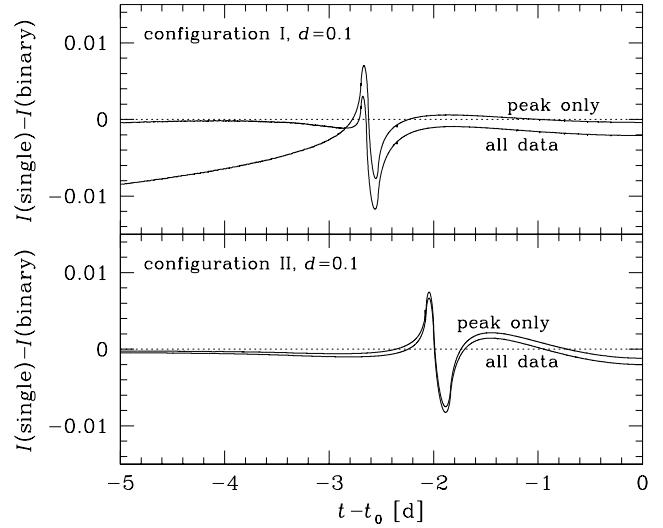


Figure 6. Differences in the light curve between a binary-lens model and a best-matching single lens model. Comparison between fits for the full data set (bold lines) and those where only the peak region ($-3 \text{ d} \leq t \leq 3 \text{ d}$) has been included (thin lines) with $\sigma_0 = 0.3\%$ for both discussed configurations and a binary separation $d = 0.1$.

is indicated. However, if one accounts for a possible 20 % increase in the size of the photometric errors, the models with $d = 0.1$ for both configurations still survive. In any case, the $d = 0.1$ models are not recommended for rejection for the larger systematic errors $\sigma_0 = 0.5\%$ or $\sigma_0 = 1\%$ by means of a χ^2 test over the peak region.

Figure 6 shows a comparison of the differences between the binary-lens and the single-lens light curves of fits involving the full data set and those restricted to the peak region for a binary-lens separation parameter $d = 0.1$. While the differences between these

Table 6. Best-matching single-lens models to the peak region of binary-lens light curves for both discussed configurations and different angular lens separations.

	$\sigma_0 = 0.3\%$					
	configuration I			configuration II		
	$d = 0.2$	$d = 0.15$	$d = 0.1$	$d = 0.2$	$d = 0.15$	$d = 0.1$
χ^2_{\min}	1121.4	926.8	461.9	3468.21	948.98	572.34
d.o.f.	398	398	398	398	398	398
$\chi^2_{\min}/\text{d.o.f.}$	2.82	2.32	1.16	8.7	2.38	1.44
$\sqrt{2\chi^2_{\min} - \sqrt{2n-1}}$	19.2	14.9	2.20	55.1	15.4	5.6
$P(\chi^2 \geq \chi^2_{\min})$	$\lesssim 10^{-81}$	$\lesssim 10^{-49}$	0.015	$\lesssim 10^{-661}$	$\lesssim 10^{-53}$	$\lesssim 10^{-8}$
t_E	90.68	58.51	56.01	34.02	34.47	34.92
u_0	0.0140	0.0181	0.0159	0.0478	0.0487	0.497
ρ_*	0.0332	0.0487	0.0495	0.0829	0.0802	0.0758
g	0.571	0.031	0.011	0.0034	0.0014	0.0005
Γ_I	1.000	0.663	0.531	1.000	1.000	0.605

Results of fits of single-lens models to the peak region ($-3 \text{ d} \leq t \leq 3 \text{ d}$) of the simulated binary-lens data sets for both configurations for a systematic error $\sigma_0 = 0.3\%$ and different angular lens separations. The parameters of the underlying binary-lens models can be found in Table 1. In contrast to the fits that include the full data set, the baseline magnitude I_{base} has been fixed, whereas the blending parameter g has been allowed to vary. Again, the free parameter t_0 fulfilled $|t_0| \lesssim 90 \text{ s}$ in all cases.

two types of fits are negligible for configuration II, the apparent differences for configuration I demonstrate the amount of information contained in the region before the first and after the last contact of the stellar limb with the caustic. For configuration I, the maximal deviation is reduced from 1.2% to 0.8% for the peak-only fits in the peak region at the cost of a deviation of up to 1.4% outside compared to 0.2% when the full data set is considered.

Given the problems in rejecting single-lens models by means of a χ^2 test, it seems to be a good idea to look for characteristic deviation patterns in order to decide on whether a model is in agreement with the observed data. An underestimate of error bars is not a problem for the assessment of a run test, which recognizes the sign of the residuals only, but not their size. In this sense, it is complementary to the χ^2 test, which is sensitive to the absolute value of the residuals, but blind to their signs. Although the obtained χ^2_{\min} may look appropriate, a model is not acceptable if it fails a run test. Let a 'run' be defined as the longest contiguous sequence of residuals with the same sign, and let N denote the total number of data points, N_+ the number of points with positive residuals, and N_- the number of points with negative residuals. For $N > 10$, the distribution of the number of runs n_r can be fairly approximated by a normal distribution with the expectation value

$$\mathcal{E}(n_r) = 1 + \frac{2N_+N_-}{N} \quad (18)$$

and the standard deviation

$$\sigma(n_r) = \sqrt{2N_+N_- \frac{2N_+N_- - N}{N^2(N-1)}}. \quad (19)$$

The goodness-of-fit can then be measured by the probability $P_r = P(n_r \leq n_r^{\text{obs}})$. In addition to n_r , other statistics such as the length of the longest run or the symmetry between N_+ and N_- may be checked.

For the fits to the full data sets whose parameters are listed in Tables 4 and 5, Tables 7 and 8 show the result of the corresponding run tests over the full light curve and over the peak region only. Requiring an associated probability $P_r \geq 0.05$ only lets the single-lens models for $d = 0.1$ and $\sigma = 1\%$ or $\sigma = 0.5\%$ for both configurations survive, while also the model for $d = 0.15$ and $\sigma = 1\%$ for configuration I nearly makes it to the acceptable region if $P_r \geq 0.01$

has to be fulfilled. If one looks at the difference between single and binary-lens light curves, one sees that it becomes undetectable as soon as it is overshadowed by the statistical spread of the data which appears to be the case for $d = 0.1$ and $\sigma_0 = 1\%$. In fact, the χ^2 test is not limited by this effect, but in principle allows to detect signals below the noise level by means of a sufficiently large number of independent measurements.

The simulations show that single lens models for the discussed configurations involving a K or M Bulge giant look acceptable for $d = 0.1$, unless the photometric uncertainties are pushed significantly below the 1%-level. The corresponding offset in the limb-darkening coefficient of $\sim 10\%$ implies that the assumption of a single lens is incompatible with the desire of a precision measurement on Γ . In contrast, the effect on the time-scale t_* is below 1%, so that potential lens binarity does not have a significant effect on the measurement of the proper motion $\mu = \theta_*/t_*$, given that the uncertainty in θ_* is much larger. One might want to argue that the binary lens system is an unlikely configuration. However, $d = 0.1$ means a projected separation $a_p = 0.2 \text{ AU}$ for configuration I with two lens stars of mass $M/2 \sim 0.18 M_\odot$ and $a_p = 0.3 \text{ AU}$ for configuration II with two lens stars of mass $M/2 \sim 0.35 M_\odot$ which should not a-priori be discarded.

4 FINAL CONCLUSIONS AND SUMMARY

Generally speaking, the potential binarity of the lens limits the accuracy of a limb-darkening measurement of the observed source star for close-impact microlensing events. The caustic near the center of the lens star is never exactly point-like, but always a small diamond with four cusps. If a point lens is assumed, the obtained limb-darkening coefficient is systematically offset, while the nature of the lens binarity may not be apparent. Although the inclusion of a binary lens in the modelling of the event will yield a proper limb-darkening measurement, the additional degrees of freedom still diminish the achievable precision. Unfortunately, such a computation is extremely demanding. Simulations for typical event configurations involving K or M Bulge giants show that single-lens models for binary lens events that involve an offset of $\sim 10\%$ on the limb-darkening coefficient Γ look acceptable both from χ^2 and from run

Table 7. Results of run tests for the best-matching single-lens models for configuration I.

		$\sigma_0 = 0.3\%$			$\sigma_0 = 0.5\%$			$\sigma_0 = 1\%$		
		$d = 0.2$	$d = 0.15$	$d = 0.1$	$d = 0.2$	$d = 0.15$	$d = 0.1$	$d = 0.2$	$d = 0.15$	$d = 0.1$
$N = 2155$ (all data)	N_+	911	1013	1051	935	1034	1063	1016	1053	1071
	N_-	1244	1142	1104	1220	1121	1092	1139	1102	1084
	$\mathcal{E}(n_r)$	1052.8	1074.6	1077.8	1059.7	1076.7	1078.3	1075.0	1077.9	1078.5
	$\sigma(n_r)$	22.7	23.1	23.2	22.8	23.2	23.2	23.1	23.2	23.2
	n_r^{obs}	365	774	1064	523	928	1086	816	1032	1122
	δ	30.4	13.0	0.60	23.5	6.4	-0.33	11.2	1.98	-1.88
	P_r	$\lesssim 10^{-202}$	$\lesssim 10^{-38}$	0.275	$\lesssim 10^{-122}$	$\lesssim 10^{-10}$	0.630	$\lesssim 10^{-28}$	0.024	0.970
$N = 404$ (peak only)	N_+	187	183	197	169	179	195	164	186	199
	N_-	217	221	207	235	225	209	240	218	205
	$\mathcal{E}(n_r)$	201.9	201.2	202.9	197.6	200.4	202.8	195.9	201.7	203.0
	$\sigma(n_r)$	10.0	10.0	10.0	9.8	9.9	10.0	9.7	10.0	10.4
	n_r^{obs}	111	120	190	123	152	198	152	178	204
	δ	9.1	8.2	1.28	7.6	4.9	0.48	4.5	2.4	-0.10
	P_r	$\lesssim 10^{-19}$	$\lesssim 10^{-15}$	0.100	$\lesssim 10^{-14}$	$\lesssim 10^{-6}$	0.317	$\lesssim 10^{-5}$	0.009	0.541

For the fits of single-lens models to the full data set corresponding to configuration I and different values of the lens separation d and the systematic error σ_0 whose parameters are displayed in Table 4, run tests over the whole data set or the peak region ($-3 \text{ d} \leq t \leq 3 \text{ d}$) revealed N_+ positive and N_- negative residuals, where ‘positive’ means that the observed magnification exceeds the theoretical one. $\mathcal{E}(n_r)$ denotes the expected number of runs and $\sigma(n_r)$ denotes the corresponding standard deviation. For n_r^{obs} runs being found, the deviation in units of $\sigma(n_r)$ becomes $\delta = [\mathcal{E}(n_r) - n_r^{\text{obs}}]/\sigma(n_r)$, which corresponds to a probability $P_r = P(n_r \leq n_r^{\text{obs}})$.

Table 8. Results of run tests for the best-matching single-lens models for configuration II.

		$\sigma_0 = 0.3\%$			$\sigma_0 = 0.5\%$			$\sigma_0 = 1\%$		
		$d = 0.2$	$d = 0.15$	$d = 0.1$	$d = 0.2$	$d = 0.15$	$d = 0.1$	$d = 0.2$	$d = 0.15$	$d = 0.1$
$N = 1741$ (all data)	N_+	888	852	846	869	850	841	856	856	839
	N_-	853	889	905	872	891	900	885	885	902
	$\mathcal{E}(n_r)$	871.2	871.1	870.8	871.5	871.0	870.5	871.3	871.3	870.4
	$\sigma(n_r)$	20.9	20.9	20.8	20.9	20.9	20.8	20.9	20.9	20.8
	n_r^{obs}	665	776	852	729	828	884	810	862	884
	δ	9.9	4.6	0.90	6.8	2.1	-0.65	2.9	0.44	-0.66
	P_r	$\lesssim 10^{-22}$	$\lesssim 10^{-5}$	0.183	$\lesssim 10^{-11}$	0.020	0.742	0.002	0.329	0.744
$N = 404$ (peak only)	N_+	218	189	200	203	187	200	196	198	196
	N_-	186	215	204	201	217	204	208	206	208
	$\mathcal{E}(n_r)$	201.7	202.2	203.0	203.0	201.9	203.0	202.8	202.9	202.8
	$\sigma(n_r)$	10.0	10.0	10.0	10.0	10.0	10.0	10.0	10.0	10.0
	n_r^{obs}	51	107	166	93	147	190	141	174	194
	δ	15.1	9.5	3.7	11.0	5.5	1.29	6.2	2.9	0.88
	P_r	$\lesssim 10^{-51}$	$\lesssim 10^{-21}$	$\lesssim 10^{-4}$	$\lesssim 10^{-27}$	$\lesssim 10^{-7}$	0.098	$\lesssim 10^{-9}$	0.002	0.189

Results of run tests corresponding to fits of single-lens models to the full data set corresponding to configuration II and different values of the lens separation d and the systematic error σ_0 whose parameters are displayed in Table 5, where either the whole data set or the peak region ($-3 \text{ d} \leq t \leq 3 \text{ d}$) has been used. The quantities shown are the same as in Table 7.

tests, unless photometry significantly below the 1 %-level is possible. The measurement uncertainty of the proper motion $\mu = \theta_*/t_*$ however is dominated by the determination of the angular source radius θ_* , involving stellar spectra, compared to which the accuracy limits on t_* caused by lens binarity for close-impact microlensing events are negligible.

In contrast, the measurement of limb darkening from fold-caustic passages does not suffer from any of the problems encountered for close-impact events. A binary lens is assumed a-priori, but the measurement of limb darkening only depends on a smaller set of local properties rather than on the complete binary-lens parameter space. The use of the local approximation of the light curve in the vicinity of the fold-caustic passage (e.g. Albrow et al. 1999c; Dominik 2004b) makes the computation quite inexpensive

and easy. Moreover, fold-caustic exits can be well predicted. Once a caustic entry has been observed, it is clear that a corresponding exit will occur, and the light curve on the rise to the caustic exit peak allows to predict the time of the caustic exit with sufficient precision usually more than a day in advance. A fair coverage of the caustic entry as well as the determination of the spectral type of the source star and an early measurement of the event time-scale t_E even allows a rough guess on the passage duration and therefore a proper a-priori assessment of the potential for measurements of the source brightness profile. While the characteristic properties of a fold-caustic exit, which provides a full scan of the source from the leading to the trailing limb, can therefore be estimated in advance, corresponding predictions for close-impact events are only possible after the leading limb has already passed the caus-

tic, leaving only the second half of the caustic passage involving the trailing limb. From fold-caustic passages, a linear limb-darkening coefficient can be obtained routinely and easily with a precision of less than 5 % (e.g. Dominik 2004c). Hence, events involving fold-caustic passages turn out to be the clear favourite over close-impact events for measuring limb-darkening coefficients apart from those where the source transits a cusp. The latter provide an opportunity to determine further limb-darkening coefficients beyond a linear law, which is quite challenging and usually impossible for fold-passage events (Dominik 2004a).

However, events with fold-caustic passages make the worse case for proper motion measurements. Fits to the light curve in the vicinity of the caustic passage only yield $t_{\star}^{\perp} = t_{\star}/(\sin \phi)$ (e.g. Afonso et al. 1998; Albrow et al. 1999c; Dominik 2004b), where ϕ is the caustic-crossing angle, which needs to be determined from a model involving the full set of binary lens parameters. While a precise measurement of t_{\star}^{\perp} is possible, the uncertainty in t_{\star} is severely limited by degeneracies and apparent ambiguities for the caustic-crossing angle ϕ (Dominik 1999; Albrow et al. 1999a; Afonso et al. 2000), which can have a comparable or even larger influence on the determination of the proper motion μ than uncertainties in the angular stellar radius θ_{\star} .

REFERENCES

- Abe F., et al., 2003, A&A, 411, L493
 Abt H. A., 1983, ARA&A, 21, 343
 Afonso C., et al., 1998, A&A, 337, L17
 Afonso C., et al., 2000, ApJ, 532, 340
 Albrow M. D., et al., 1998, ApJ, 509, 687
 Albrow M. D., et al., 1999a, ApJ, 522, 1022
 Albrow M. D., et al., 1999b, ApJ, 522, 1011
 Albrow M. D., et al., 1999c, ApJ, 512, 672
 Albrow M. D., et al., 2000, ApJ, 534, 894
 Albrow M. D., et al., 2001, ApJ, 549, 759
 Albrow M. D., et al., 2002, ApJ, 572, 1031
 Alcock C., et al., 1997, ApJ, 491, 436
 Asada H., 2002, A&A, 390, L11
 Bogdanov M. B., Cherepashchuk A. M., 1995, Astronomy Reports, 39, 779
 Bogdanov M. B., Cherepashchuk A. M., 1996, Astronomy Reports, 40, 713
 Di Stefano R., 2000, ApJ, 541, 587
 Dominik M., 1998, A&A, 333, L79
 Dominik M., 1999, A&A, 349, 108
 Dominik M., 2004a, MNRAS, 352, 1315
 Dominik M., 2004b, MNRAS, 353, 69
 Dominik M., 2004c, MNRAS, 353, 118
 Dominik M., et al., 2002, P&SS, 50, 299
 Dominik M., Hirshfeld A. C., 1994, A&A, 289, L31
 Dominik M., Hirshfeld A. C., 1996, A&A, 313, 841
 Fields D. L., et al., 2003, ApJ, 569, 1305
 Gaudi B. S., Gould A., 1999, ApJ, 513, 619
 Gould A., 1994, ApJ, 421, L71
 Gould A., Welch D. L., 1996, ApJ, 464, 212
 Heyrovský D., 2003, ApJ, 594, 464
 Heyrovský D., Sasselov D., Loeb A., 2000, ApJ, 543, 406
 Mao S., Paczynski B., 1991, ApJ, 374, L37
 Milne E. A., 1921, MNRAS, 81, 361
 Nemiroff R. J., Wickramasinghe W. A. D. T., 1994, ApJ, 424, L21
 Paczynski B., 1986, ApJ, 304, 1
 Rhie S. H., Bennett D. P., 1999, Line Caustic Microlensing and Limb Darkening, astro-ph/9912050
 Schechter P. L., Mateo M., Saha A., 1993, PASP, 105, 1342
 Schneider P., Wagoner R. V., 1987, ApJ, 314, 154
 Schneider P., Weiß A., 1987, A&A, 171, 49
 Schramm T., Kayser R., 1987, A&A, 174, 361
 Tsapras Y., Horne K., Kane S., Carson R., 2003, MNRAS, 343, 1131
 Udalski A., 2003, Acta Astronomica, 53, 291
 Udalski A., et al., 1994, Acta Astronomica, 44, 165
 Udalski A., Szymanski M., Mao S., Di Stefano R., Kaluzny J., Kubiak M., Mateo M., Krzeminski W., 1994, ApJ, 436, L103
 Witt H. J., 1995, ApJ, 449, 42
 Witt H. J., Mao S., 1994, ApJ, 430, 505
 Witt H. J., Mao S., 1995, ApJ, 447, L105
 Yoo J., et al., 2004, ApJ, 603, 139